Evaluating the effects of detector angular misalignments on simulated computed tomography data

Massimiliano Ferrucci [a,b,*], Evelina Ametova [b], Simone Carmignato [c], Wim Dewulf [b]

[a] Engineering Measurement Division, National Physical Laboratory, Hampton Road, Teddington TW11 0LW, Middlesex, United Kingdom
[b] Department of Mechanical Engineering, KU Leuven, Celestijnenlaan 300—Box 2420, 3001 Leuven, Belgium
[c] Department of Management and Engineering, Università degli Studi di Padova, Stradella San Nicola 3, 36100 Vicenza, Italy

ABSTRACT

The quality of dimensional measurements made by industrial X-ray computed tomography (CT) depends on a variety of influence factors in the measurement process. In this paper, the effects of angular misalignments of a flat-panel detector are investigated. First, a forward projection model is applied to evaluate distortions of the radiographic pixel coordinates assigned to X-ray intensities due to various detector rotation angles. Distortion maps are presented for a set of representative detector rotations and the sensitivity of image distortions to each rotation is discussed. It is shown from a simulation study that detector angular misalignments result in systematic errors of the reconstructed volume. The distortion model is inversely applied to generate correction maps that are used to correct the simulated radiographs from a misaligned detector. A new volume is reconstructed from the corrected radiographs and the new deviations are compared to the uncorrected results. The reduction of observed volumetric errors after radiographic correction validates the efficacy of the radiographic distortion model. Additionally, the output of this study can contribute to the development of a geometrical error model for volumetric measurements made by CT.

Crown Copyright © 2016 Published by Elsevier Inc. All rights reserved.

1. Introduction

In X-ray CT, the accurate reconstruction of the measurement volume is strongly dependent on the alignment of the system geometry [1]. For typical industrial CT systems, the geometry is defined by the relative position and orientation of the three main components [2], namely the X-ray source (particularly, the X-ray focal spot), rotation axis, and detector. To determine the sensitivity of the reconstructed volume to the alignment of these three components, the principles of X-ray CT are briefly revisited here.

The measurement volume is reconstructed by way of applying tomographic (slice-wise) reconstruction to a collection of radiographic images—or radiographs [3]. Typically, radiographs are taken in sequence as a test object is rotated on a stage. The information contained within each radiograph corresponds to the spatial distribution of attenuated X-rays incident on the plane of the detector. More specifically, the intensity registered by each pixel corresponds to the intensity of those X-rays that traverse the path

from the X-ray source to the corresponding pixel. In the case of an object within the measurement volume, the registered intensity at each pixel will depend on the attenuation of X-rays by the object along the source-to-pixel path. The intensity at each pixel will also depend on scatter and other X-ray effects that are out of the scope of this paper, but are discussed elsewhere in the literature [3].

Radiographs are taken at multiple rotation positions, providing a denser sampling of X-ray attenuation trajectories through the measurement volume. The registered attenuation along all X-ray paths is used by the reconstruction algorithm to generate a three-dimensional distribution of relative attenuation values in the measurement volume. This volumetric model consists of three-dimensional pixels, 'voxels', with assigned grey values, which correspond to the relative attenuation at that voxel position. The position of each voxel is given by the three-dimensional coordinates of its centre. Subsequent processing of the volumetric data, such as segmentation and surface sampling, can be used to generate a three-dimensional point cloud; dimensional measurements can then be performed on the resulting coordinate points [1].

The accuracy of the extracted three-dimensional coordinates is dependent on the alignment of the system geometry and its stability during a scan. The grey value assigned to a voxel representing a particular volumetric space is calculated from

* Corresponding author at: National Physical Laboratory, Hampton Road, Teddington TW11 0LW, Middlesex, United Kingdom. Tel.: +44 20 8943 7018.
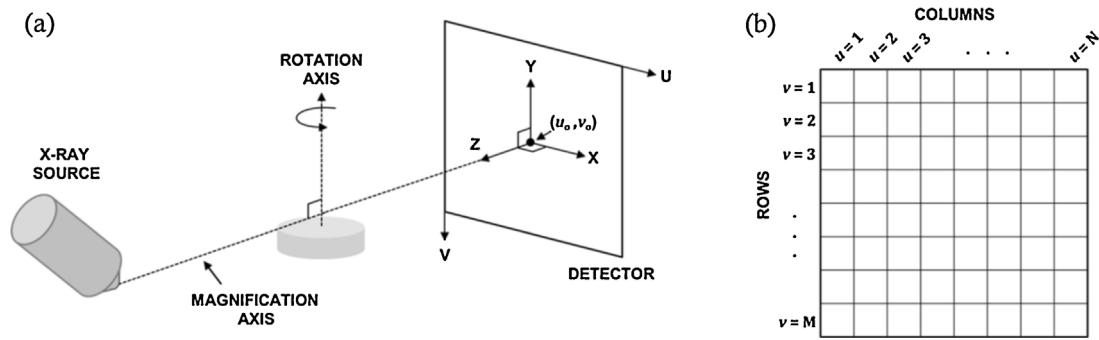 *E-mail address:* massimiliano.ferrucci@npl.co.uk (M. Ferrucci).

(a)

(b)

Fig. 1. (a) The ideal geometrical alignment of a typical industrial cone-beam X-ray CT system. (b) The pixel column indices increase rightward, while the pixel row indices increase downward. The pixel position $(u, v) = (1, 1)$ is located at the top left corner of the detector.

the set of X-ray trajectories through that volumetric space. Each trajectory through the measurement volume is determined from the assumed positions of source and pixel. Also, knowledge of the relative orientation of the measured object between radiographs is determined from the rotation of the stage, which is typically assumed to be stable [2]. Deviations in the system geometry from its assumed state will introduce errors in the radiographic pixel coordinates assigned to registered X-ray intensities. The propagation of these errors through the reconstruction algorithm will result in errors of the binning of grey values to individual voxels and, consequently, errors in dimensional measurements performed on the reconstructed volume.

In this paper, the effects of angular misalignments of a flat-panel detector on volumetric measurements made by CT are studied. First, the geometry of a typical cone-beam X-ray CT system is described. Then, a forward projection model [4] is adapted to generate radiographic distortion maps for various detector rotations. In practice, uncertainty in the input parameters would result in an uncertainty of the distortion maps. The scope of this study is to evaluate the effects of a misaligned detector; therefore, the input parameters for the model are assumed to be exactly known. It is shown by simulation that detector angular misalignments result in systematic dimensional errors of the reconstructed volume. The simulation study is briefly discussed and the volumetric errors are presented for various detector misalignments. The distortion model is then applied inversely to correct the radiographs from each simulated detector misalignment. A new, corrected volume is reconstructed with the corrected radiographs. The deviations from ideal geometry in the corrected volumes are compared to the deviations in the corresponding uncorrected volumes.

2. Instrument geometry

Fig. 1a summarizes the X-ray CT instrument geometry assumed for this paper. To begin, a right-handed global coordinate system is defined. The magnification axis, also the Z axis, is given by the line connecting the centre of the X-ray focal spot to the centre of the detector. The Y axis is parallel to the rotation axis of the object stage. The X axis is orthogonal to both the Y and Z axes, thus forming a Cartesian coordinate system. The origin is defined as the intersection of the ideal magnification axis and the detector plane. The positive Z direction is towards the X-ray source, while the positive Y direction is upwards (opposite the direction of gravity). The direction of the positive X axis follows the right-hand rule. The X-ray source-to-rotation axis distance (SRD) is given by the distance from the centre of the X-ray focal spot to the intersection of the rotation and magnification axes, while the source-to-detector distance (SDD) is given by the distance from the X-ray focal spot centre to the centre of the detector. Both SRD and SDD are positive values. The detector is positioned on the opposite side of the rotation stage

from the source, thus SDD is larger than SRD. SRD is not an input parameter to the model but is mentioned here for reference.

The nominal alignment of the detector is as follows. The magnification axis (Z) is normal to the plane of the detector. The vertical axis of the detector (V) is antiparallel to the Y-axis, while the horizontal axis of the detector (U) is parallel to the X-axis. The flat panel detector consists of M by N pixels, where M is the number of rows and N is the number of columns (Fig. 1b). Ideally, the pixels are equally-sized and equally-spaced in the plane of the detector; the variables Δu and Δv correspond to the pixel width and height, respectively. The centre of each pixel in the detector is assigned column (u) and row (v) indices. The ($u, v = (1, 1)$ position is at the top left corner of the detector screen; the columns increase rightward (+X direction in the system coordinate frame), while the rows increase downward ($-Y$ direction in the system coordinate frame). The variables u_o and v_o are the pixel column and row coordinates, respectively, corresponding to the intersection of the magnification axis and the detector; this feature is also known as the principal point—a term commonly found in camera calibration for machine vision [5]. In the case of an ideally aligned detector, the principal point is located at the geometrical centre of the detector plane. Depending on the number of pixel rows and columns (even or odd), the centre of the detector can fall on a pixel or on the edge between adjacent pixels, i.e. u_o and v_o can be non-integer values.

Angular misalignments of the detector are described by three rotations: detector tilt θ about the X-axis (Fig. 2, left), detector slant φ about the Y-axis (Fig. 2, centre), and detector skew η about the Z-axis (Fig. 2, right). Tilt θ and slant φ are known as out-of-plane rotations, while skew η is an in-plane rotation. Detector rotations, in practice, are not constrained to occur about the central axes of the detector plane [6]; such rotations can be modelled as a combination of detector translation and rotation.

The effects of positional misalignments of the detector are not investigated in this paper to allow for in-depth analysis of angular misalignments. The principal point is therefore located at the detector centre. It should be noted, however, that the radiographic error model presented here includes parameters for positional misalignments of the detector. Positional misalignments in X and Y can be modelled by adapting the principal point u_o and v_o, whereas a misalignment in Z is modelled by adapting SDD.

A detector can be misaligned by more than one rotation angle simultaneously. Various established conventions may be used for rotating three-dimensional coordinates [7]; these conventions differ by the axes about which the rotations are performed and the sequence in which the axes are rotated. In general, the application of different conventions will not generate equivalent final three-dimensional rotations. The convention used here is chosen to agree with the convention used to simulate a rotation of the detector in the analytical (ray-tracing) simulation software Scorpius XLab®. More information on Scorpius XLab® can be found in the literature
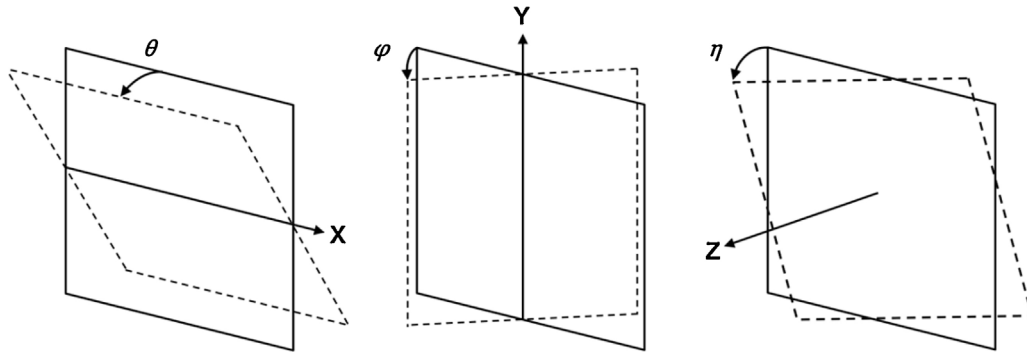
Fig. 2. Potential detector angular misalignments include tilt θ (left), slant φ (middle), and in-plane skew η (right). Positive rotations are illustrated.

[8]. All rotations are extrinsic and are performed about the fixed *X*, *Y*, and *Z* axes of the global coordinate frame. The positive direction of rotation is given by the right-hand screw rule (see Fig. 2).

3. Radiographic distortions

Radiographic or pixel distortion is defined as the shift in the pixel coordinates assigned to registered point intensities (X-ray photons) from the image plane of an aligned detector to the image plane of a misaligned detector. The intensity of incident X-rays is registered by pixel (u, v) in the aligned detector. On a misaligned detector, the same X-ray intensity is registered by pixel (u_r, v_r), as depicted in Fig. 3.

The difference in registered pixel position from the aligned detector plane to the misaligned detector plane corresponds to the pixel distortion for the pixel (u, v) in the aligned detector plane and is given by the following equation:

$$\mathrm{d}u = u_r - u, \quad \mathrm{d}v = v_r - v \tag{1}$$

Principles of forward projection may be adapted to evaluate the pixel distortion in the presence of various representative detector rotations. Similarly to the derivation provided by Yang et al. [4], the calculation of d*u* and d*v* is achieved by the following steps. First, the (x, y, z) coordinates of each pixel centre in the aligned detector are determined. Then, a set of straight lines from the X-ray focal spot centre (given by a point) to the coordinates of each pixel centre are generated. The intersections of the straight lines with the now misaligned detector plane are subsequently determined. For each
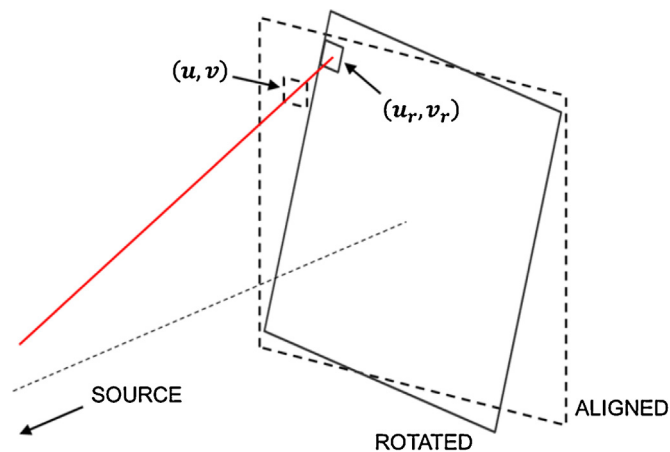

Fig. 3. An incident X-ray photon will be registered at different pixel coordinates on the aligned and rotated detectors [(u, v) and (u_r, v_r), respectively]. In this diagram, the rotated detector is a result of multiple rotations.

Table 1
The non-varying geometrical parameters describing the CT system.

Geometrical parameter	Value
Detector size	400 mm × 400 mm
Number of pixels ($M \times N$)	2000 × 2000
Pixel size ($\Delta u \times \Delta v$)	0.2 mm × 0.2 mm
SRD	350 mm
SDD	1700 mm

intersection point on the rotated detector, the corresponding column and row indices (u_r, v_r) are extracted. Finally, d*u* and d*v* are evaluated for each pair of (u_r, v_r) and (u, v).

Distortion maps may be generated for various out-of-plane rotations θ and φ and in-plane rotations η. It is important to note that the magnitude of detector rotations studied in this paper is significantly larger than experimentally observed rotations in test systems. Nevertheless, the magnitudes are chosen to clearly present the geometrical behaviour in the radiographic distortions. The values of other non-varying geometrical input parameters used in the model are given in Table 1. The magnitude of the total distortion, *i.e.* $\sqrt{\mathrm{d}u^2 + \mathrm{d}v^2}$, is plotted in colour for each pixel. The direction of the distortion vector is given by the superimposed arrows (decimated by 80 for clarity). Distortion statistics are presented for each applied rotation in Table 2.

3.1. Out-of-plane rotations θ and φ

Distortion maps are presented for $\theta = +5°$, +10° in Fig. 4 and for $\varphi = +5°$, +10° in Fig. 5. In the case of a detector tilt θ, distortion increases for rows further from mid-plane (row v_o). Distortion is, to first approximation, constant for all *u* in a given *v*. Note that the trend of distortion increase for rows away from v_o is not symmetrical about v_o, as might be expected. Further, the general trend for constant distortion across a row is modified by the local minimum, which is evident on the vertical centerline of the distortion plot for each test rotation in Fig. 4. The pixel distortions point towards the local minimum for pixel rows occupying the same image half as the local minimum. Equal and opposite rotations have mirrored

Table 2
Maximum, mean, and standard deviation σ of the distortion magnitudes in the presence of various detector rotations.

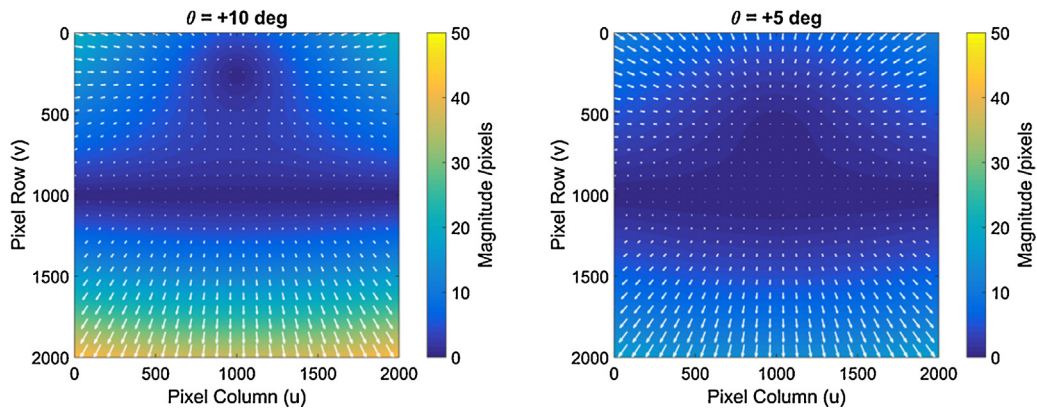| Rotation		Distortion magnitude (pixels)		
		Maximum	Mean	σ
θ or φ	±10°	42.5	10.9	10.0
	±5°	17.6	4.7	4.0
η	±2°	49.3	26.7	9.9
	±1°	24.7	13.4	5.0

Fig. 4. Distortion maps for varying values of θ. Note the direction of U and V.
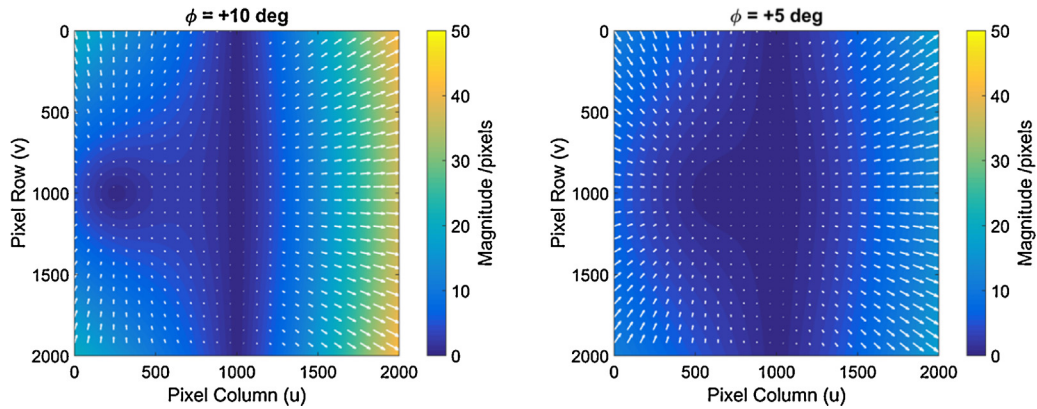

Fig. 5. Distortion maps for varying values of φ. Note the direction of U and V.

distortions about the horizontal centre line in the case of detector tilt θ and about the vertical centre line in the case of detector slant φ. Due to the simplified nature of the modelled geometry, distortions due to detector slant φ can be expected to correspond to distortions for tilts θ, but mirrored in the line $u = v$.

The presence of local minima along the image centre lines can be explained by the diagram in Fig. 6a, in which an X-ray path to a detector with tilt θ is shown on the YZ plane. The X-ray path from the source intersects the rotated detector at v_r and the ideal detector at v. The dotted arc has a radius of v and connects the two pixel row positions v_r and v. Therefore, $v_r = v$ and the pixel row distortion d$v = 0$. Also, since the diagram is on the YZ plane, d$u = 0$ (see Fig. 4). Therefore, the total distortion for that particular pixel row is zero. The row position of this minimum changes with the magnitude of θ, as is shown by the diagonal zero line in Fig. 6b. In

this figure, the horizontal zero line corresponds to the X-axis and the vertical zero line is the distortion when $\theta = 0$.

3.2. In-plane rotation η

Distortion maps in the presence of in-plane rotation $\eta = +1°$, $+2°$ are presented in Fig. 7. The magnitude of distortions increases with increasing distance from the detector centre. As expected, the distortion direction at any pixel position is tangent to the radial direction; that is, the distortions follow a circular trajectory with the detector centre at the trajectory centre.

Table 2 summarizes the magnitude of the distortion for various detector rotations.

The distortions in the presence of $\eta = \pm 1°$ and $\eta = \pm 2°$ are larger than the distortions in the presence of $\theta = \varphi = \pm 5°$ and $\theta = \varphi = \pm 10°$,
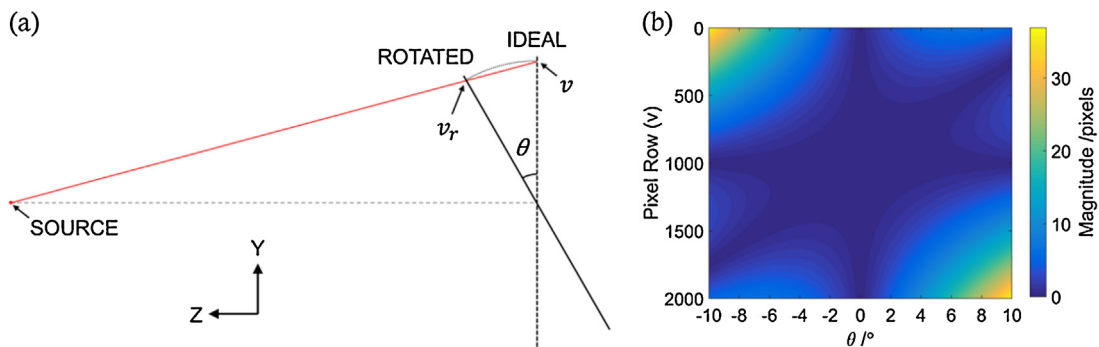

Fig. 6. (a) X-ray path diagram along YZ plane. Given detector tilt θ, there exists an X-ray path that will be registered by the same pixel coordinate in both the ideal and rotated detectors. (b) The pixel row position for this occurrence depends on the value of θ, as is shown by the diagonal zero line.
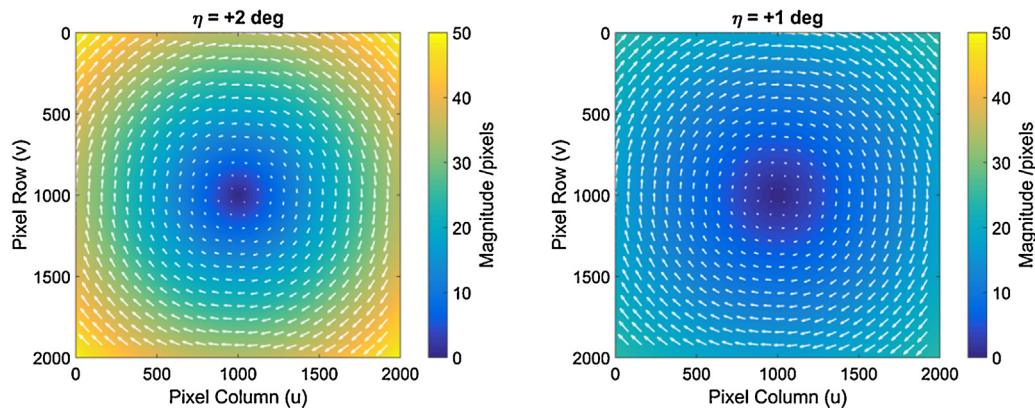
Fig. 7. Distortion maps for varying values of η. Note the direction of *U* and *V*.

respectively. The sensitivity of distortion magnitude to rotation angle is depicted by Fig. 8, in which maximum and mean distortion magnitude is plotted as a function of rotation angle.

4. Volumetric deviations

The effects of angular misalignments of the detector are studied on simulated CT scans of a test object. A cone-beam CT system is simulated using Scorpius XLab®. The system geometry is characterized by the parameters in Table 1. The current of the X-ray source is set to 0.1 mA and the voltage is set to 100 kV. The test object is a computer-modelled cylindrical array of aluminium spheres (Fig. 9). One hundred and twenty five spheres are separated into five layers along the cylindrical axis. Each layer consists of twenty four spheres arranged in three concentric circles and one additional sphere located at the common centre. The diameter of the modelled spheres is 5 mm.

The test object is placed within the system such that its cylindrical axis is coincident with the axis of rotation and its centre (the central sphere of layer C) is coincident with the intersection of the rotation and magnification axes. In this position and orientation, the third layer of spheres is centred on the mid-plane (*XZ*); thus, two of the layers are below this mid-plane and two are above it. For the purpose of isolating the effects of geometrical errors, other influence factors, such as finite X-ray focal spot size, focal spot drift, and electronic noise and MTF of the detector, were not simulated. The test object is imaged at 3600 equally-spaced rotation positions over a range of 360°; the number of projections was chosen to reduce the effects of insufficient projection data. Subsequent to collecting
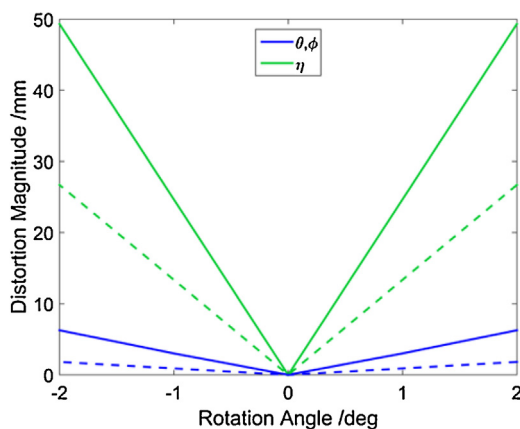
the full set of radiographs, the volume is reconstructed by filtered backprojection (Feldkamp type) algorithms [9] included in the simulation software. Default settings for performing reconstruction in Scorpius XLab® were used. Prior to the backprojection step, a Shepp-Logan filter [10] is applied to the radiographic data. Bilinear interpolation [3] is performed in the backprojection step. The number of voxels in the reconstructed volume are 1999, 2000, and 1999 along *X*, *Y*, and *Z*, respectively. Voxel dimensions are 40.9 μm along *X* and *Z* and 36.4 μm along *Y*.

Surfaces in the three-dimensional voxel model are determined by applying a grey value threshold between the material of interest (aluminium) and the background (air). Advanced (local) thresholding on VGStudio MAX with a search distance of 0.15 mm is performed on a starting grey value, which was chosen to provide a single continuous surface for each sphere object. The surface is subsequently converted to a three-dimensional point cloud by way of sampling the isosurface at intervals of 0.08 mm along all three coordinate directions (using the surface extraction feature in VGStudio MAX). For each sphere object in the point cloud, the centre of mass (centroid) of all surface points is calculated. It should be noted that sphere fitting is not used in determining the centroid of the sphere object; it is shown later in this paper that certain detector orientations resulted in form deviations of the scanned spheres. For this purpose, the form of the reconstructed spheres is also used to understand the effects of detector misalignments. Other studies [11] use the volumetric grey value data to evaluate the centroid of the sphere objects. This method eliminates the surface determination step, thereby removing the effects of thresholding [12] on the centroid results. Here, surface data is used as it is necessary to evaluate the form of the reconstructed spheres. Spheres are linear least-squared fit to each object and the root-mean-square (RMS) value of sphere fit residuals is used as the criterion for form deviation. It should be noted that other definitions for sphere form exist. The centroid and form deviation evaluated under each detector misalignment are compared to the same features obtained under ideal system geometry. Feldkamp artifacts due to insufficient radon data at large cone-beam angles [13] could affect the centroid calculation. Given that both misaligned and ideal scan data are affected by Feldkamp artifacts, their influence is not considered.

4.1. Detector tilt, θ

The following tilts of the detector about the *X*-axis are simulated: $\theta = +10°$, $+5°$, $-5°$, and $-10°$. In Fig. 10, centroid deviations are presented as vectors superimposed on the nominal centroid positions. The deviation vectors are scaled by a factor of 20 for visualization in the measurement volume. Centroid deviations are not symmetrical about the *XZ* mid-plane. A local minimum is evident

Fig. 8. Maximum (solid line) and mean (dotted line) pixel distortion magnitude as a function of rotation angle for θ, φ, and η.
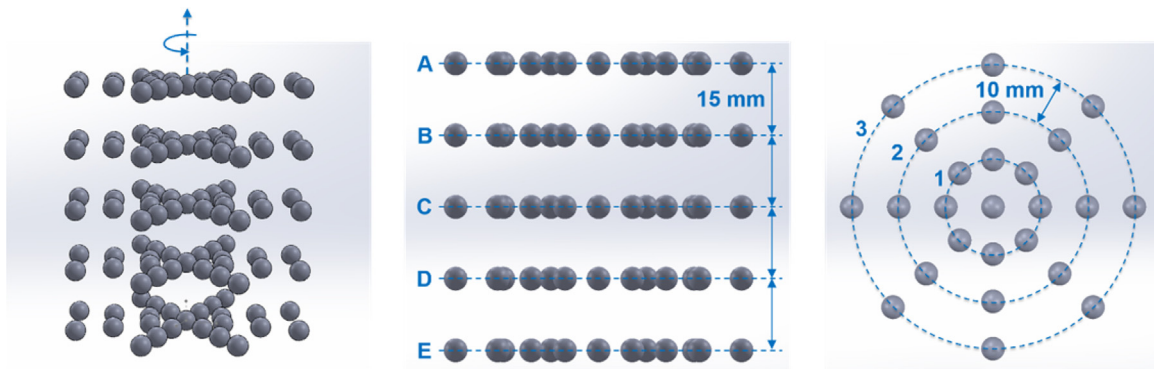
Fig. 9. A cylindrical array of aluminium spheres was modelled for the purpose of sampling the measurement volume. (Left) 3D view, (centre) lateral view, (right) top-down view.

Table 3
Mean centroid deviation magnitude by sphere layer in the presence of detector tilt θ.

θ	Layer A	Layer B	Layer C	Layer D	Layer E
+10°	0.29	0.19	0.01	0.38	0.99
+5°	0.19	0.07	0.01	0.14	0.38
−5°	0.38	0.14	0.01	0.07	0.19
−10°	0.99	0.38	0.01	0.19	0.29

above the mid-plane for positive tilt angles and below the mid-plane for negative tilts. This behaviour corresponds to the local minimum observed in Fig. 4. The data in Table 3 confirms the non-symmetrical behaviour about the mid-plane. Deviations due to equal and opposite rotations are mirrored about the XZ plane.

4.2. Detector slant, φ

The following slants of the detector about the Y-axis are simulated: $\varphi = +10°$, +5°, −5°, and −10°. The deviations in centroid coordinates for the cases $\varphi = +10°$ and $\varphi = −10°$ are plotted in Fig. 11; the magnitude of plotted deviations is scaled by a factor of 20 for visualization in the measurement volume. The results for $\varphi = \pm5°$ exhibit the same behaviour as the $\varphi = \pm10°$ cases, respectively, only at smaller magnitudes; for this reason, the $\varphi = \pm5°$ plots are not presented. Horizontal (XZ) deviations are radially outward, i.e. away from axis of rotation and vertical (Y) deviations point towards the mid-plane (Fig. 11, centre). The magnitude of deviations generally increases with increasing distance of the sphere from the axis of rotation; this behaviour is evident from the data in Table 4.

4.3. Detector skew, η

The following skews of the detector about the Z-axis are simulated: $\eta = +2°$, +1°, −1°, and −2°. The centroid deviation diagram is not shown for detector skew since the deviation vectors were not noticeable at a scaling factor of 20. Instead, the statistics for

Table 4
Mean centroid deviation magnitude by distance from rotation axis in the presence of detector slant φ.

φ	Centre	Ring 1	Ring 2	Ring 3
+10°	0.01	0.13	0.26	0.34
+5°	0.02	0.04	0.06	0.08
−5°	0.01	0.04	0.06	0.08
−10°	0.01	0.13	0.26	0.34

centroid deviation due to each detector rotation are summarized in Table 5.

A closer look at the reconstructed volume suggests that centroid deviation is not the most suitable criterion for determining the effects of detector skew. The reconstructed volumes in the presence of detector tilt $\theta = +10°$, detector slant $\varphi = +10°$, and detector skew $\eta = +2°$ are presented, respectively, in Fig. 12 top, centre, and bottom. On the left, a grey-value slice along the XY plane (prior to the application of a surface threshold) is shown. A magnified portion of the grey-value image is shown in the centre of Fig. 12; in the presence of detector slant and skew, the sphere object is reconstructed as two overlapping sphere objects, each individually having a lower material attenuation value than the overlapping section. An appropriate grey-value threshold is applied to generate a surface for the overlapping portion, as this section has comparable grey-values to the ideally-reconstructed sphere objecfts. A three-dimensional view of the reconstructed sphere objects after grey-value thresholding is presented in Fig. 12, right.

As a result of the behaviour observed in Fig. 12 and the magnitude of centroid deviations in Table 5, form deviation seems to be a more appropriate criterion to determine the complete effects of detector slant φ and detector skew η. Given the symmetrical behaviour observed in Table 5, form deviation statistics are only shown for positive rotation angles (Table 6). The results support the sensitivity statements made in Section 3. Also, detector slant contributes more strongly to form deviations than detector tilt.

4.4. Multiple rotations

CT scans in the presence of multiple detector rotations are simulated. The first three combinations included rotations about two

Table 5
Maximum, mean, and standard deviation of centroid deviation magnitude for all sphere objects in the presence of detector rotations.

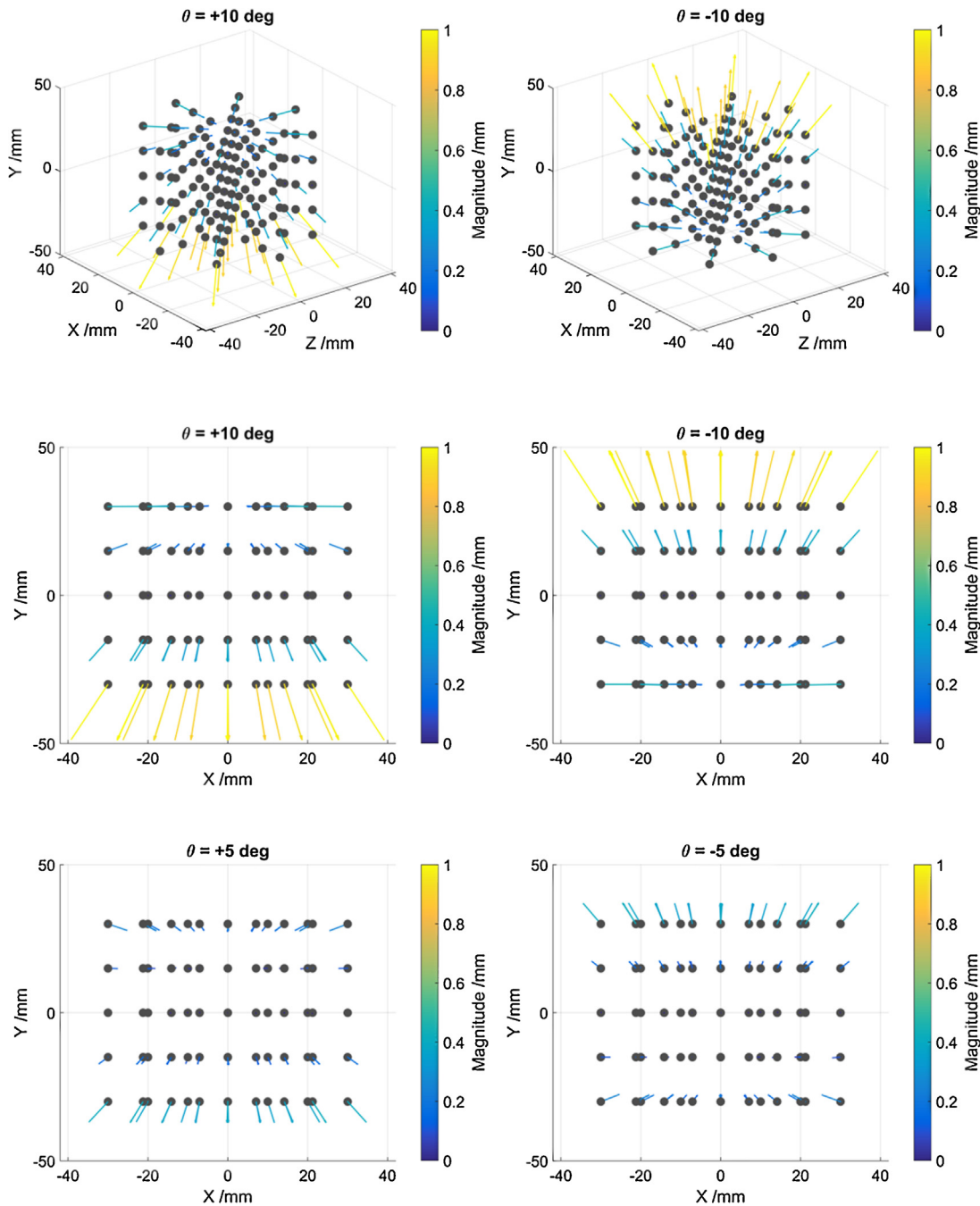| Rotation		Centroid deviation magnitude/mm		
		Maximum	Mean	σ
θ	+10°	1.05	0.37	0.34
	+5°	0.42	0.16	0.13
	−5°	0.42	0.16	0.13
	−10°	1.04	0.37	0.34
φ	+10°	0.40	0.23	0.10
	+5°	0.10	0.06	0.02
	−5°	0.10	0.06	0.02
	−10°	0.40	0.23	0.10
η	+2°	0.11	0.04	0.03
	+1°	0.04	0.02	0.01
	−1°	0.04	0.01	0.01
	−2°	0.11	0.04	0.03

Fig. 10. Centroid deviations in the presence of detector tilt θ. Deviation vectors are scaled by a factor of 20 for visualization.

Table 6

The root-mean-square of the sphere fit residuals over all spheres in the volume is used as criterion for form deviation. Here the mean and standard deviation σ of the RMS are shown for positive values of each detector angle. Maximum values are omitted due to the presence of noise particles, which result in outliers of the surface data.

Rotation		RMS of sphere fit residuals/mm	
		Mean	σ
θ	+10°	0.02	0.02
	+5°	0.01	2.66×10^{-3}
φ	+10°	0.10	0.06
	+5°	0.05	0.04
η	+2°	0.23	0.07
	+1°	0.13	0.04

axes, while the last two combinations included rotations about all three axes. Negative rotations are covered in the final three-axis combination.

$(\theta, \varphi, \eta) = (+5, +5, 0); (+5, 0, +1); (0, +5, +1); (+5, +5, +1); (-5, -5, -1)$

The statistics for centroid and form deviations due to multiple rotations are summarized in Table 7.

5. Radiographic correction

The authors of reference [14] observed an improvement in tomographic image quality after correcting for geometrical errors in the radiographic data. Here, the approach of correcting radiographic data prior to reconstruction is evaluated quantitatively and
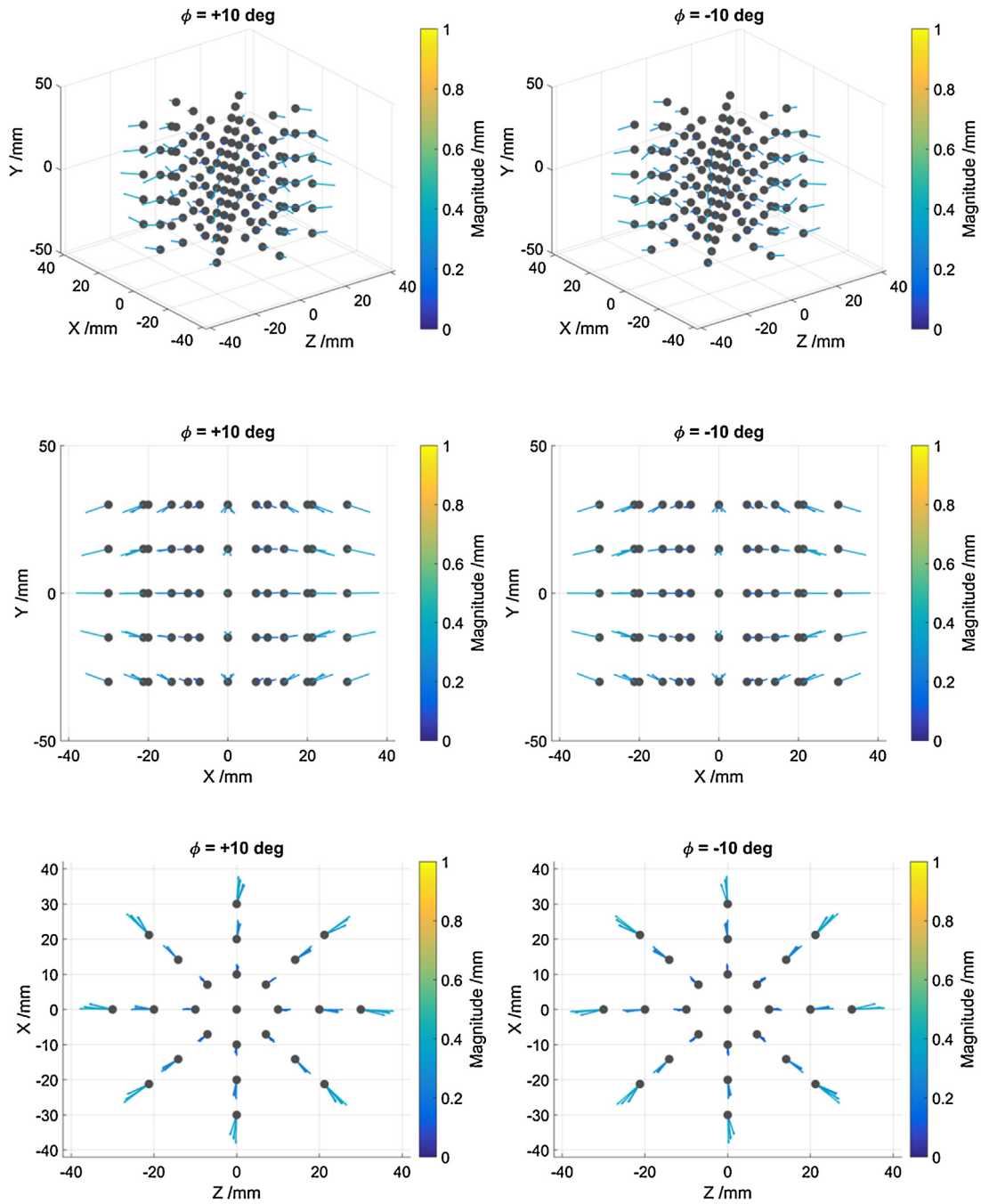
Fig. 11. Centroid deviations in the presence of various detector slants φ. Deviation vectors are scaled by a factor of 20 for visualization.

Table 7
Centroid deviation and form deviation statistics in the presence of multiple rotations.

Rotation			Centroid deviation magnitude/mm			RMS of sphere fit residuals/mm	
θ	φ	η	Maximum	Mean	σ	Mean	σ
+5°	+5°		0.44	0.16	0.13	0.06	0.03
+5°		+1°	0.42	0.16	0.13	0.13	0.04
	+5°	+1°	0.21	0.08	0.05	0.13	0.05
+5°	+5°	+1°	0.63	0.19	0.17	0.12	0.05
−5°	−5°	−1°	0.44	0.16	0.12	0.15	0.05

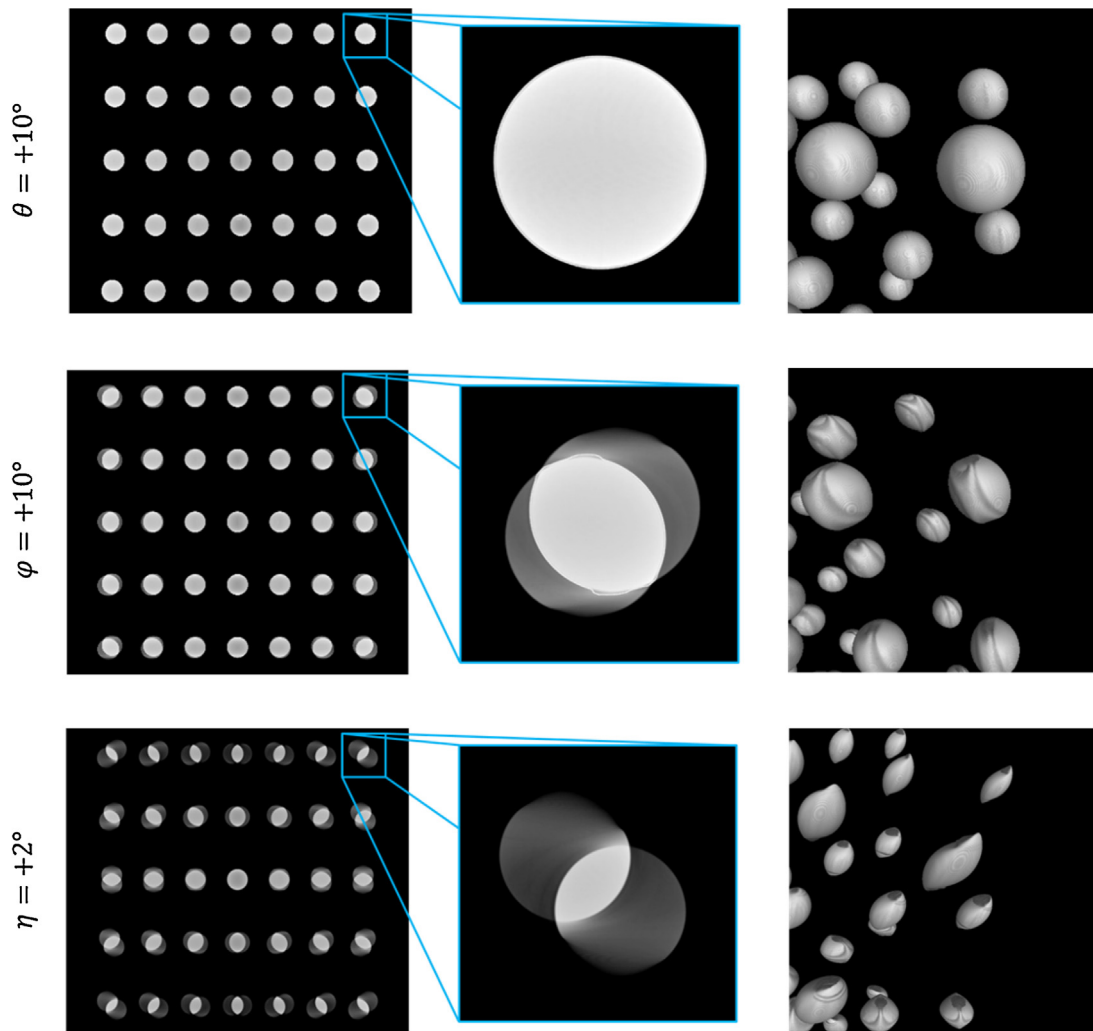**Fig. 12.** Reconstructed volume in the presence of detector tilt θ = +10°, detector slant φ = +10°, and detector skew η = +2°. Left: grey-value slice along XY-plane before grey-value thresholding. Centre: magnified portion of grey-value image. Right: three-dimensional view of the reconstructed sphere objects after applying grey-value thresholding.

in the context of reducing dimensional measurement errors. Since the approach is applied to simulated data, the angular misalignments of the detector are known precisely. In a test system, detector misalignments can be measured either with reference instruments or by imaging a reference object. Uncertainty in the experimental measurements would result in an uncertainty of the applied correction.

Distortion correction maps were generated for each simulated detector misalignment and applied to the corresponding radiographic data. Correcting the radiograph consists of shifting the pixel position assigned to an intensity value by an amount corresponding to the distortion correction at that pixel position. The *imwarp* function in MATLAB's image processing toolbox is used to perform the re-binning of intensity data for all radiographs. The function includes options for interpolating the shifts between pixels; linear interpolation was used in this study. As an example, a radiograph taken with a detector skew η = +2° is shown in Fig. 13, left; the imaged cylindrical array is slightly tilted. To ensure that the border pixels are preserved after the correction procedure, the radiographic images were initially padded by 50 pixel on each side with repeated border intensity values. The result of not padding the image data prior to correction is shown in Fig. 13, centre. The intensities from the original border pixels are shifted inward towards the centre of the image. Since there is no data to replace the border

pixels, they are automatically assigned a zero intensity value. As a result of the padding step, it is important that the border pixels only include background (air) intensity data. Subsequent to padding the image and applying the pixel shifts, the image is cropped back to its original size (Fig. 13, right).

New volumes are reconstructed from the corrected radiographs. The same procedures defined in Section 4 for determining centroid and form deviations are used here.

5.1. Individual rotations

The statistics for centroid deviation in the corrected volumes are presented for individual rotations in Table 8. Form deviation statistics are summarized for positive individual rotations in Table 9. The percentage change from the uncorrected form deviation is also presented.

5.2. Multiple rotations

The statistics for centroid deviation in the corrected volumes are presented for multiple rotations in Table 10. Sphere form statistics are summarized for positive multiple rotations in Table 11. The percentage change from the uncorrected sphere form is also presented.
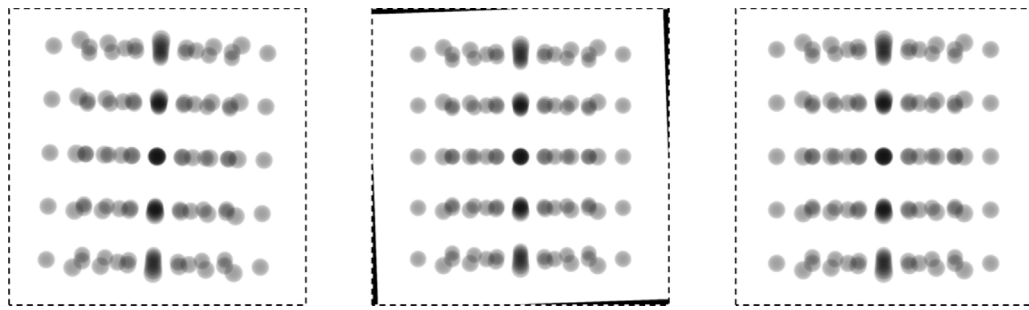
Fig. 13. The pixel positions assigned to intensity values in the original radiograph are shifted according to the distortion correction map for the given detector misalignments. Left: The original radiograph in the presence of a skew $\eta = 2°$; notice the tilted orientation of the imaged cylindrical array. Centre: Result of not padding the radiograph before performing correction. Intensity values for border pixels are shifted inward, while there are no intensity values to replace to occupy the original pixels—thus, those 'empty' border pixels are assigned zero intensity. (Right) The result of shifting the pixels after padding and subsequent cropping.

Table 8
Maximum, mean, and standard deviation σ of centroid deviation magnitude for individual rotations after radiographic correction. The percent change from the uncorrected deviation values is also shown.

Angles		Centroid deviation after correction/mm					
		Maximum	Change (%)	Mean	Change (%)	σ	Change (%)
θ	+10°	5.73×10^{-2}	−94.5	1.76×10^{-2}	−95.3	1.42×10^{-2}	−95.8
	+5°	2.39×10^{-2}	−94.3	9.64×10^{-3}	−93.9	4.27×10^{-3}	−96.7
	−5°	2.21×10^{-2}	−94.8	9.55×10^{-3}	−93.9	3.72×10^{-3}	−97.1
	−10°	5.37×10^{-2}	−94.9	1.65×10^{-2}	−95.5	1.37×10^{-2}	−96.0
φ	+10°	3.28×10^{-2}	−91.8	1.34×10^{-2}	−94.2	6.32×10^{-3}	−93.9
	+5°	1.97×10^{-2}	−80.8	9.14×10^{-3}	−84.4	3.83×10^{-3}	−83.9
	−5°	2.70×10^{-2}	−74.1	9.61×10^{-3}	−83.7	4.35×10^{-3}	−82.4
	−10°	3.13×10^{-2}	−92.2	1.34×10^{-2}	−94.2	5.73×10^{-3}	−94.5
η	+2°	7.19×10^{-2}	−36.2	3.70×10^{-2}	+3.0	1.27×10^{-2}	−55.6
	+1°	2.61×10^{-2}	−30.8	1.32×10^{-2}	−14.1	5.26×10^{-3}	−30.8
	−1°	2.67×10^{-2}	−33.4	1.32×10^{-2}	−11.3	5.03×10^{-3}	−31.0
	−2°	6.72×10^{-2}	−38.8	3.70×10^{-2}	+3.1	1.30×10^{-2}	−55.9

Table 9
Mean and standard deviation σ of the RMS of sphere fit residuals over all spheres for individual rotations after radiographic correction. The percent change from the uncorrected RMS values is also shown.

Angles		RMS of sphere fit residuals after correction/mm			
		Mean	Change (%)	σ	Change (%)
θ	+10°	2.82×10^{-3}	−82.8	6.59×10^{-4}	−96.0
	+5°	2.58×10^{-3}	−59.3	3.85×10^{-4}	−85.5
φ	+10°	2.77×10^{-3}	−97.1	6.03×10^{-4}	−99.0
	+5°	2.44×10^{-3}	−94.7	2.91×10^{-4}	−99.2
η	+2°	2.48×10^{-3}	−98.9	3.92×10^{-4}	−99.4
	+1°	2.44×10^{-3}	−98.1	3.16×10^{-4}	−99.3

Table 10
Maximum, mean, and standard deviation σ of centroid deviation magnitude for multiple rotations after radiographic correction. The percent change from the uncorrected deviation values is also shown.

Angles			Centroid deviation after correction/mm					
θ	φ	η	Maximum	Change (%)	Mean	Change (%)	σ	Change (%)
+5°	+5°		2.51×10^{-2}	−94.3	1.13×10^{-2}	−92.8	4.61×10^{-3}	−96.4
+5°		+1°	3.03×10^{-2}	−92.7	1.12×10^{-2}	−92.9	4.90×10^{-3}	−96.1
	+5°	+1°	3.27×10^{-2}	−84.5	1.41×10^{-2}	−82.5	6.31×10^{-3}	−87.2
+5°	+5°	+1°	2.30×10^{-2}	−96.4	1.11×10^{-2}	−94.1	4.10×10^{-3}	−97.6
−5°	−5°	−1°	4.64×10^{-2}	−89.4	1.60×10^{-2}	−90.0	8.44×10^{-3}	−93.2

Table 11
Mean and standard deviation of the RMS of sphere fit residuals over all spheres for multiple rotations after radiographic correction. The percent change from the uncorrected RMS values is also shown.

Angles			RMS of sphere fit residuals/mm			
θ	φ	η	Mean	Change (%)	σ	Change (%)
+5°	+5°		2.58×10^{-3}	−95.8	3.32×10^{-4}	−98.9
+5°		+1°	2.55×10^{-3}	−98.0	3.89×10^{-4}	−99.1
	+5°	+1°	2.58×10^{-3}	−98.1	3.57×10^{-4}	−99.3
+5°	+5°	+1°	2.66×10^{-3}	−97.7	4.62×10^{-4}	−99.1
−5°	−5°	−1°	2.78×10^{-3}	−98.2	4.49×10^{-4}	−99.1

6. Conclusion

A forward projection model [4] is adapted to evaluate distortions in the pixel coordinates assigned to X-ray intensity data due to angular misalignments of a detector. It is observed in this study that the magnitude of pixel distortions is more sensitive to detector rotations about the Z-axis (skew, η) than about the X- or Y-axes. For example, in the presence of detector tilt $\theta = 10°$ (about the X-axis) or detector slant $\varphi = 10°$ (about the Y-axis), the maximum distortion was 42.5 pixel; a detector skew $\eta = 2°$ resulted in a maximum distortion of 49.3 pixel. Similarly, the average distortion over the entire 2000×2000 pixel image space was 10.9 pixel in the presence of detector tilt $\theta = 10°$ or detector slant $\varphi = 10°$; the average distortion in the presence of detector skew $\eta = 2°$ was 26.7 pixel.

Commercial software Scorpius XLab® is used to simulate CT scans of a computer generated cylindrical array of aluminum spheres. Scans are simulated under ideal geometry and in the presence of various detector misalignments. Centroid position and sphere form in the reconstructed volumes are used as criteria for evaluating the effects of detector misalignments on the measurement volume. It is shown that tilts of the detector about the X axis contributed mostly to centroid deviations; these deviations generally increased with increasing distance of the sphere from the mid-plane. On the other hand, detector slants about the Y axis contributed significantly to both centroid and sphere form deviations; the effects of detector slant increased with increasing sphere distance from the rotation axis. Detector skew about the Z axis contributed mostly to sphere form deviation; the effects of detector skew increased with increasing distance from the centre of the volume. Systematic deviations observed in the volumetric data can be used to inform the development of dedicated reference objects for estimating detector misalignments in a test system.

The distortion model is applied inversely to correct radiographic data from a misaligned detector. New volumes are reconstructed from the corrected radiographs and the centroid and form deviations are compared to the uncorrected values. After distortion correction, deviations in centroid position in the presence of detector tilt were reduced by 93% to 97%, while deviations due to detector slant were reduced by 74% to 94%. On the other hand, deviations in centroid position due to detector skew are reduced by 30% to 40%. The RMS of sphere fit residuals was reduced by 95% to 99% in the presence of detector slant and skew, while it was reduced by 50% to 80% in the presence of detector tilt. Similar reductions were observed for the data in the presence of multiple detector rotations. The observation of such reductions validates the efficacy of the radiographic distortion model presented in this paper.

The methodology presented here can be useful for a user to correct for detector rotations in their CT system, without requiring involvement from the instrument manufacturer. However, several limitations exist. For example, the proposed method assumes the values of the detector rotations are known in advance. Some methods to determine detector position and orientation exist in the literature [2]. Additionally, to enable corrections, measurements should be avoided at the extremities of the reconstructed volume; that is, the projection of the measured object should not occupy the border pixels of the radiographic image (see Section 5). Finally, the radiographic correction procedure has been validated under strictly-controlled, *e.g.* noiseless, simulation conditions. There is concern that pixel interpolation used in the re-binning of radiographic intensities (the MATLAB function *imwarp*, in this study) could result in loss of valuable projection data. An alternative method to correct for known geometric misalignments involves modifying the geometrical parameters used in the backprojection

step of the reconstruction algorithm [15]. However, the ability to modify the reconstruction algorithm is currently limited to very experienced users.

The model used to generate the correction maps assumes that input parameters are exactly known. In practice, uncertainty in the input parameters will influence the output of the correction methodology. If the model is applied to generate correction maps, the uncertainty in the input parameters will propagate into uncertainty in the applied corrections. The same is true if the tomographic reconstruction algorithm is modified. Uncertainty in the CT geometry used to backproject radiographic intensities will result in uncertainty of the position and intensity of the reconstructed grey values. To ensure traceability of measurements, all error sources must be accounted for and their contribution to measurement uncertainty must be quantified in a traceable way. Therefore, it is important that any input parameter be calibrated, *i.e.* measured in a traceable manner with a statement of uncertainty. However, while methods to measure instrument geometry exist [2], a dedicated calibration procedure is not yet available.

Future work includes experimentally applying the correction methodology to a test system with detector rotations. Other pixel interpolation methodologies in the radiographic re-binning step will be investigated to reduce potential data loss. Future research includes investigating the applicability of modified tomographic reconstruction algorithms to reduce the effects of a misaligned CT system. Uncertainty in the applied corrections is an important step to assessing measurement uncertainty in CT; therefore, the evaluation of this uncertainty is also considered in future work.

References

[1] Kruth JP, Bartscher M, Carmignato S, Schmitt R, De Chiffre L, Weckenmann A. Computed tomography for dimensional metrology. CIRP Ann—Manuf Technol 2011;60:821–42, http://dx.doi.org/10.1016/j.cirp.2011.05.006.

[2] Ferrucci M, Leach RK, Giusca CL, Dewulf W, Carmignato S. Towards geometrical calibration of X-ray computed tomography systems—a review. Meas Sci Technol 2015:26, http://dx.doi.org/10.1088/0957-0233/26/9/092003.

[3] Buzug TM. Computed tomography: from photon statistics to modern cone-beam CT. Berlin: Springer-Verlag; 2008.

[4] Yang K, Kwan ALC, Miller DF, Boone JM. A geometric calibration for cone-beam CT systems. Med Phys 2006;33:1695–706.

[5] Hartley R, Zisserman A. Multiple view geometry in computer vision. 2nd ed. Cambridge, UK: Cambridge University Press; 2003.

[6] Sun Y, Hou Y, Zhao F, Hu J. A calibration method for misaligned scanner geometry in cone-beam computed tomography. NDT E Int 2006;39:499–513, http://dx.doi.org/10.1016/j.ndteint.2006.03.002.

[7] Weisstein EW. Euler angles. From MathWorld—A Wolfram Web Resource n.d. ⟨http://mathworld.wolfram.com/EulerAngles.html⟩ (accessed June 15, 2015).

[8] Hiller J, Reindl LM. A computer simulation platform for the estimation of measurement uncertainties in dimensional X-ray computed tomography. Measurement 2012;45:2166–82, http://dx.doi.org/10.1016/j.measurement.2012.05.030.

[9] Feldkamp LA, Davis LC, Kress JW. Practical cone-beam algorithm. J Opt Soc Am 1984;1:612–9.

[10] Shepp LA, Logan BF. The fourier reconstruction of a head section. IEEE Trans Nucl Sci 1974;NS-21:21–43.

[11] Kumar J, Attridge A, Wood PKC, Williams MA. Analysis of the effect of cone-beam geometry and test object configuration on the measurement accuracy of a computed tomography scanner used for dimensional measurement. Meas Sci Technol 2011;22:035105, http://dx.doi.org/10.1088/0957-0233/22/3/035105, http://dx.doi.org/10.1088/0957-0233/22/3/03.

[12] Ontiveros S, Yagüe JA, Jiménez R, Brosed F. Computer tomography 3D edge detection comparative for metrology applications. Procedia Eng 2013;63:710–9, http://dx.doi.org/10.1016/j.proeng.2013.08.263.

[13] Grass M, Köhler T, Proksa R. 3D cone-beam CT reconstruction for circular trajectories. Phys Med Biol 2000;45:329–47.

[14] Stevens GM, Saunders R, Pelc NJ. Alignment of a volumetric tomography system. Med Phys 2001;28:1472, http://dx.doi.org/10.1118/1.1382609.

[15] Sun Y, Hou Y, Hu J. Reduction of artifacts induced by misaligned geometry in cone-beam CT. IEEE Trans Biomed Eng 2007;54:1461–71, http://dx.doi.org/10.1109/TBME.2007.891166.